

Scaling Law for Impact Resistance of Amorphous Alloys Connecting Atomistic Molecular Dynamics with Macroscale Experiments

Yujie Cheng,[○] Jinlei Dong,[○] Fucheng Li,[○] Yidi Shen, Qi An, Kailu Xiao, Minqiang Jiang, Yanhui Liu, Chenguang Huang, Xianqian Wu,^{*} and William A. Goddard, III^{*}



Cite This: *ACS Appl. Mater. Interfaces* 2023, 15, 13449–13459



Read Online

ACCESS |



Metrics & More



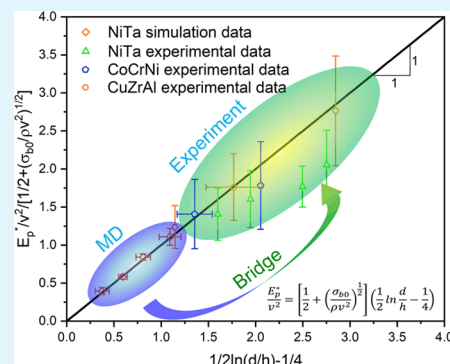
Article Recommendations



Supporting Information

ABSTRACT: Establishing scaling laws for amorphous alloys is of critical importance for describing their mechanical behavior at different size scales. In this paper, taking Ni₂Ta amorphous metallic alloy as a prototype materials system, we derive the scaling law of impact resistance for amorphous alloys. We use laser-induced supersonic micro-ballistic impact experiments to measure for the first time the size-dependent impact response of amorphous alloys. We also report the results of molecular dynamics (MD) simulations for the same system but at much smaller scales. Comparing these results, we determined a law for scaling both length and time scales based on dimensional analysis. It connects the time and length scales of the experimental results on the impact resistance of amorphous alloys to that of the MD simulations, providing a method for bridging the gap in comparing the dynamic behavior of amorphous alloys at various scales and a guideline for the fabrication of new amorphous alloy materials with extraordinary impact resistance.

KEYWORDS: scaling law, amorphous alloy, micro-ballistic impact, dimensional analysis, molecular dynamics simulation



INTRODUCTION

High-performance materials with excellent impact resistance are essential to developing dramatically improved protective engineering.^{1–3} Understanding the dynamic mechanical response at different sizes is of critical importance for the design of protective structures and the fabrication of materials with extraordinary impact resistance. However, it is challenging to obtain the scaling effects of the mechanical behavior of materials at different scales due to size effects.^{4,5} In this paper, we bridge the gap in comparing the impact resistance of amorphous alloy materials at the micro-ballistic impact experimental scale and the atomistic level of molecular dynamics (MD) simulations.

For the development of high-performance protective materials, amorphous alloys have attracted considerable attention in recent years.^{6,7} The disordered atomic-level structure renders excellent properties such as ultrahigh strength, high hardness, and unique fracture toughness,^{8–10} making amorphous alloys promising for applications as bulletproof materials.¹¹ A Whipple shield structure consisting of an amorphous alloy coating showed much higher impact resistance under hypervelocity impact compared to the traditional Whipple shields due to the higher density, lower specific heat, and relatively low temperature of the amorphous alloy.^{11–13} Similarly, using metallic glasses as intermediate layers increased significantly the impact-protective performance of the Whipple structure.¹² With decreasing the thickness to nanoscale, the 60-nm-thick Ni₆₀Ta₄₀ amorphous alloy nanofilm exhibited excellent impact resistance subjected to micro-ballistic impact, which is

comparable to Kevlar fiber.¹³ The shear banding, cracking, and bending of cracking-induced petals are the main energy dissipation modes beyond the localized perforated hole, which is strongly dependent on impact velocities. It is known that the strength of materials generally increases with decreasing dimensions due to the dimensional constraints at small scales.^{14–16} The impact resistance of amorphous alloy films is also expected to improve significantly upon decreasing their thickness. This raises the intriguing question: do amorphous alloy films possess a scaling law regarding impact resistance under high loading rates? If the thickness of the film is decreased to several nanometers, will the scaling law still apply at the atomistic scale?

Here, we consider the Ni₂Ta metallic glass (MG) as a model material due to its good glass-forming ability, ultrahigh strength, excellent impact resistance,¹³ and thermal stability.¹⁷ We obtain the size-dependent impact resistance of amorphous alloy nanofilms through micro-ballistic impact experiments. Then, we develop the scaling law based on dimensional analysis to describe the multiscale impact resistance of amorphous alloys. In addition, we obtain the size-dependent impact resistance of the

Received: November 2, 2022

Accepted: January 26, 2023

Published: February 7, 2023



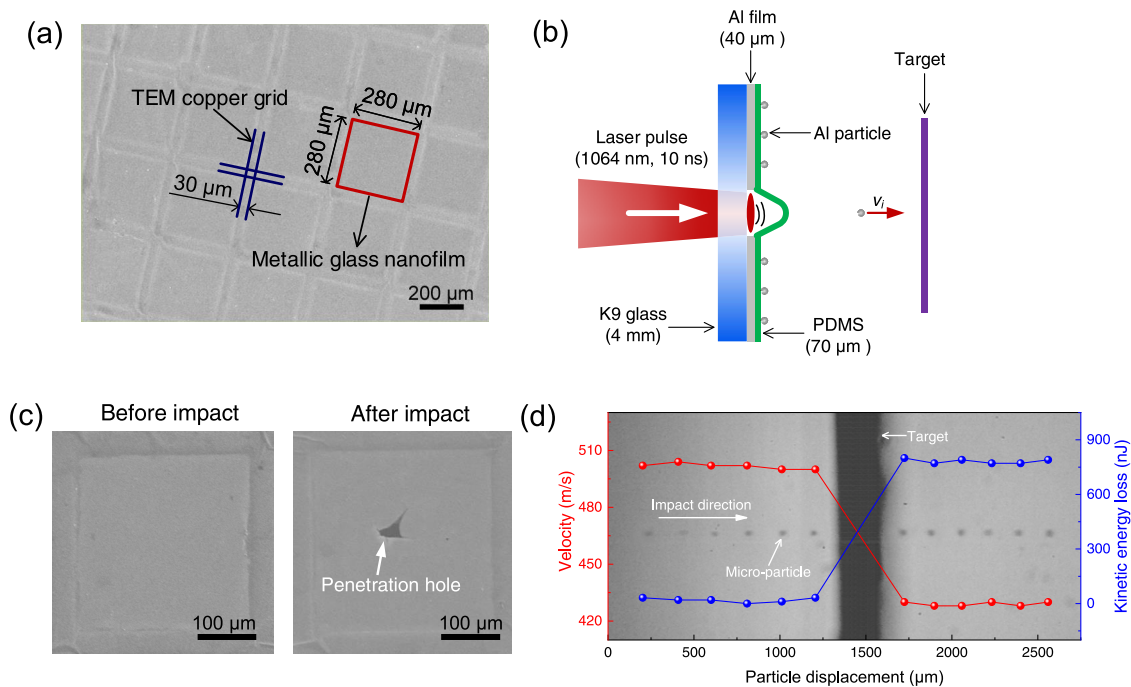


Figure 1. Laser-induced micro-particle impact testing (LIPIT) for the Ni₂Ta MG nanofilm. (a) Low-magnification SEM image showing the Ni₂Ta nanofilm supported by TEM copper grids. (b) Schematic diagram of the LIPIT platform. (c) SEM images of the Ni₂Ta nanofilm before and after perforation. (d) Multiframe snapshots show the velocity change and energy loss of the Al micro-particles during penetration at the speed of 500 m s⁻¹.

Ni₂Ta amorphous alloy film using MD simulation, from which we extract a specific formula for the scaling law. Indeed, we find that the MD-derived scaling law agrees with the experimental scaling law for several types of amorphous alloy nanofilms, indicating a universal scaling law that is applicable down to the atomistic scale. The study provides a method for predicting the multiscale impact resistance of amorphous alloys, which is of great significance for the preparation and screening of amorphous alloys with extraordinary impact resistance.

RESULTS AND DISCUSSION

Experimental Results. As a model material system for amorphous alloys, we used Ni₂Ta MG fabricated by ion-beam-assisted deposition (IBAD) attached with 100 mesh transmission electron microscopy (TEM) copper grids as the impact target (Figure 1a). To explore the size-dependent impact resistance performance of the amorphous alloy films, we built the laser-induced micro-particle impact testing (LIPIT) platform originally developed by Lee et al.¹ and further improved by Veysset et al.¹⁸ and Hassani-Gangaraj et al.,¹⁹ as illustrated in Figure 1b. It opens a window for directly studying the mechanical response and deformation behavior of nanoscale materials under extreme dynamic conditions.^{20–22} In LIPIT experiments, the nanofilms are fully perforated by the Al micro-bullets (Figure S1 and Table S1) for all impact velocities. Molecular sieves with different screening sizes are used for particle screening before the impact test to ensure uniform particle diameter. We extracted the microscale yield strength Y_d of Al under micro-particle supersonic impact to be about 308 MPa (Figure S2 and Table S2). The morphologies of the nanofilm before and after perforation were imaged in high-resolution scanning electron microscopy (SEM), as illustrated in Figure 1c. The kinetic energy loss, ΔE_k , of the micro-bullet during penetration is calculated by measuring its initial impact

velocity, v_i , and residual velocity, v_r , through the high-speed imaging system,

$$\Delta E_k = \frac{1}{2}m(v_i^2 - v_r^2) \quad (1)$$

where the mass of the micro-bullet is $m = (2.2 \pm 0.3) \times 10^{-11}$ kg (Table S1). The diameter D of micro-particle is measured by SEM image, then the particle mass is calculated by $m = 4/3\pi\rho(D/2)^3$, where ρ is the density of Al (2.7 g cm^{-3}). Figure 1d shows a typical penetration process at a high impact velocity of 500 m s⁻¹, indicating the abrupt decrease of the velocity and rapid increase of the kinetic energy loss of the micro-bullets during penetration. The Al micro-bullet keeps its spherical shape intact after penetrating through the Ni₂Ta MG nanofilm. Both the numerical simulation results (see Figure S3 in the Supporting Information) and the experimental observations confirm that the deformation and the fracture of the Al micro-bullets are negligible in the present impact velocity range. Therefore, we ignore the contribution of deformation and fracture of the Al micro-bullets to energy dissipation during the impact. In experiments, the ΔE_k consists of the energy E_p used to penetrate the MG nanofilm and the energy dissipation E_{air} due to the air drag. Since E_{air} is much lower than the corresponding ΔE_k (calculated accounting for the air-drag-induced projectile deceleration, see the Supporting Information), the air drag loss during impact is negligible. Both v_i and v_r are corrected to the values right at the front and back sides of the nanofilm.

The penetration energy E_p is rewritten as

$$E_p = (\rho A_s h) \frac{v_i^2}{2} + E_d \quad (2)$$

where ρ is the density of the Ni₂Ta MG nanofilm (13.65 g cm^{-3} , from simulations), h is the thickness of the film, and $A_s = \pi D^2/4$ is the strike-face area impacted by the spherical micro-bullet. The first term on the right-hand side of eq 2 represents the

kinetic energy transferred to the nanofilm within A_s and the second term, E_d , accounts for all other types of dissipated energy beyond A_s . To reveal the intrinsic impact resistance performance of materials, we employ the specific penetration energy, $E_p^* = E_p(\rho A_s h)^{-1}$, representing the kinetic energy dissipation per unit mass of the nanofilm. This leads to

$$E_p^* = \frac{1}{2}v_i^2 + E_d^* \quad (3)$$

where E_d^* is the delocalized penetration energy. Large delocalized penetration energy is critical for mitigating high-speed ballistic impact energy.

The E_p^* of the Ni_2Ta MG nanofilms with various thicknesses and impact velocities are measured as shown in Figure 2 (Table

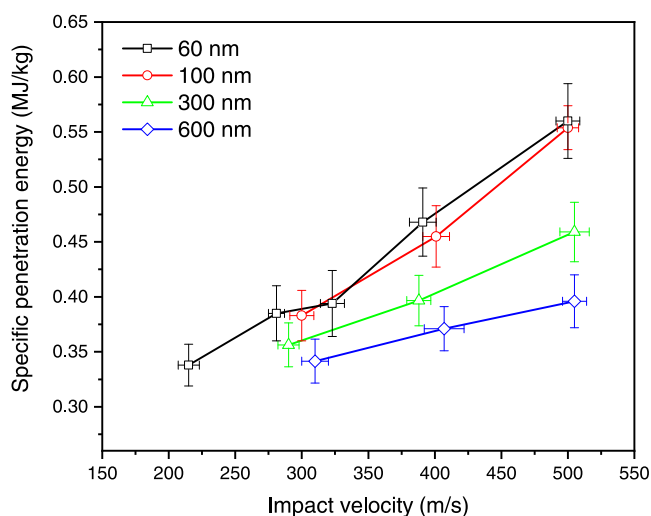


Figure 2. Specific penetration energy (E_p^*) of the Ni_2Ta MG nanofilms with different thicknesses and impact velocities in micro-ballistic impact experiments.

S3), indicating that the E_p^* increases significantly with increasing impact velocity and decreasing thickness of the nanofilm. When $v_i = 323 \text{ m s}^{-1}$, the partial overlap of results from 60-nm-thick and 100-nm-thick nanofilms results from experimental measurement uncertainties. As v_i increases from 300 to 500 m s^{-1} , E_p^* increases by about 0.055 MJ kg^{-1} for the 600-nm-thick film and by 0.18 MJ kg^{-1} for the 60-nm-thick film. For $v_i = 500 \text{ m s}^{-1}$, the E_p^* of the 60-nm-thick film¹³ is about 1.5 times that of the 600-nm-thick film, showing the size-dependent impact resistance of the nanofilm. According to eq 3, a thinner film possesses a larger delocalized energy dissipation capability. Compared with traditional impact-protective materials, the Ni_2Ta MG nanofilms show the obvious superiority of the impact resistance with higher specific penetration energy. In addition, the Ni_2Ta MG nanofilm shows an impact resistance performance comparable to that of the “armor-grade” Kevlar composite as shown in Figure S4.

The observed postpenetration features of the damage zone of the Ni_2Ta MG nanofilms with different thicknesses and impact velocities are shown in Figure 3. The damage behavior involving both the damaged area and form depends significantly on the impact velocity and the thickness of the nanofilm. For films with the same thickness, the perforation area increases with increased impact velocity. At the same impact velocity, the penetration area of the Ni_2Ta MG nanofilm increases with decreasing thickness of the film, indicating higher delocalized penetration

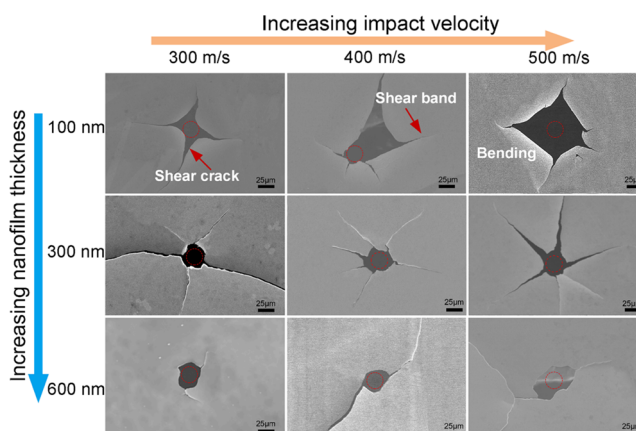


Figure 3. Postpenetration SEM images of the damage zone of the Ni_2Ta MG nanofilms with different thicknesses and impact velocities.

energy (Figure S5). The TEM images of shear bands at the shear crack of the Ni_2Ta MG nanofilms with different thicknesses indicate the basic energy dissipation mechanism (Figure S6). As shown in Figure 3, for the 100-nm-thick film, multiple cracks formed as a consequence of shear band propagation are observed around the perforation hole, resulting in several petals.²³ Unlike the plastic dissipation of crystalline solids, shear transitions (STs) can occur in MGs as basic flow events.^{24,25} With increasing impact velocity, the perforation hole enlarges with permanent bending deformation of the petals, indicating significant energy dissipation capacity by global plastic deformation of the nanofilm in addition to the localized shear bands. This behavior contrasts sharply with the bulk state, which exhibits very limited plasticity.¹⁷ With increasing the thickness to 300 nm, in addition to the localized shear bands the petals around the penetration hole resulting from the propagation of shear bands are observed. However, the bending of the petals is not obvious compared to that of the 100-nm-thick film. For the thickest 600 nm film, the penetration morphologies of the MG nanofilm are circular holes with almost the same strike area as the micro-bullet, implying a low delocalization energy dissipation capacity. It can be seen from Figure 4, that no crystallization occurs and the Ni_2Ta MG nanofilms still maintain amorphous structures after penetration.

Based on experimental results, the Ni_2Ta MG film exhibits a brittle-to-ductile transition under ballistic impact similar to crystalline materials^{15,16,26–29} with decreasing thickness from 600 to 100 nm. The failure of the 600-nm-thick film shows a typical brittle fracture of the bulk MG material,¹⁷ while the 100-nm-thick film shows obvious plasticity as evidenced by the bending of the petals. MGs generally lack inherent barriers for crack propagation such as at grain boundaries in crystalline metals and alloys. They mainly dissipate plastic energy through local shear bands³⁰ as shown in Figure 3. The formation of shear bands involves both nucleation and growth of the shear bands. The nucleation triggers the creation of new shear bands providing plastic deformation, while the growth process accelerates the destruction of MGs, leading to the ultimate fracture. Competition between energy dissipation of shear band nucleation and propagation determines the deformation behavior of MGs.³¹ As the study by Guo et al.¹⁴ and Jang et al.,¹⁶ when the sample sizes of ZrCuAlNiTi and ZrTiCoBe MGs are smaller than the characteristic critical size of about 100 nm under quasi-static loading, the dissipation energy of shear band nucleation will be less than the energy required for growth of

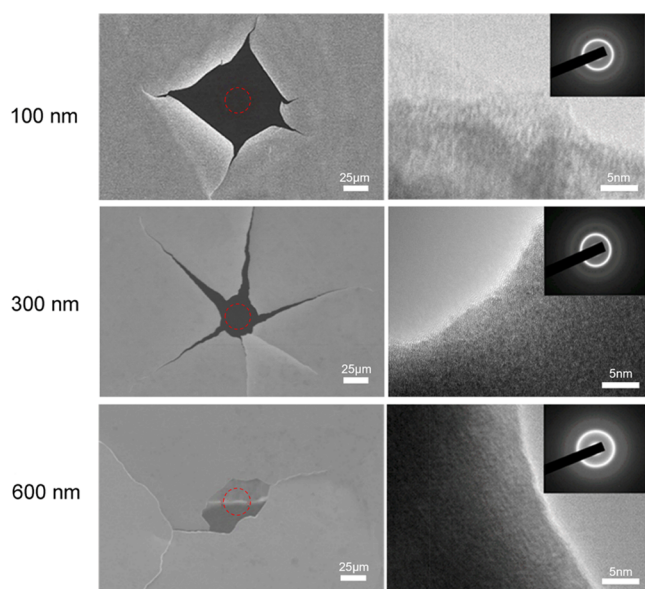


Figure 4. TEM images of fracture edges of the Ni₂Ta MG nanofilms with different thicknesses.

shear band. As a result, shear band nucleation will be more active to form multiple shear bands to exhibit ductile deformation behavior.^{16,27} As the thickness increase, shear band propagation will eventually play a dominant role, leading to localized deformation and eventually brittle fracture behavior. In the present study, the failure morphology of the Ni₂Ta MG film with a thickness of 100 nm shows shear band multiplication, which can remarkably improve the plasticity of the Ni₂Ta film. In contrast, the failure of the 600-nm-thick film shows typical brittle fracture of the bulk MG material due to the limited plasticity provided by a single shear band propagation.¹⁷ In addition, it is to be noted that the critical size of about 100 nm for brittle-to-ductile transition of the Ni₂Ta MG film under ultrahigh loading rates up to 10⁸ s⁻¹ is the same as the Zr-based MG under quasi-static loadings,¹⁴ implying that the critical size might be the same for MGs and is independent to strain rates, which will be further studied in future. The wave speed of Ni₂Ta MG nanofilm is obtained as 3580 m s⁻¹ based on the density $\rho = 13.65 \text{ g cm}^{-3}$ and elastic modulus $E = 175 \text{ GPa}$. The stress wave takes about 0.16 ns to go through the thickness of the 600-nm-thick film, which is far less than the projectile penetration time of about tens of nanoseconds. Therefore, the stress wave is in equilibrium along the thickness of the film during penetration.

MD Simulation Results. To understand the dynamic response of the Ni₂Ta films under the micro-ballistic impact, we performed molecular dynamics (MD) simulations. Figure 5 shows the MD-predicted specific penetration energy of the nanofilms for various thicknesses and impact velocities. For each thickness and impact velocity, we simulated 5 cases with an independent assignment of the Maxwell–Boltzmann velocities. This leads to a maximum error of less than 0.2 MJ kg⁻¹. As a result, the error bars are not discernable in Figure 5. It is obvious that the specific penetration energy increases quadratically with increasing impact velocity. In addition, the specific penetration energy increases quickly with decreasing thickness of the film, indicating a size-dependent impact resistance of the MG nanofilm consistent with the experimental results. For $v_1 = 8 \text{ km s}^{-1}$, the specific energy absorption of the 0.5-nm-thick MG

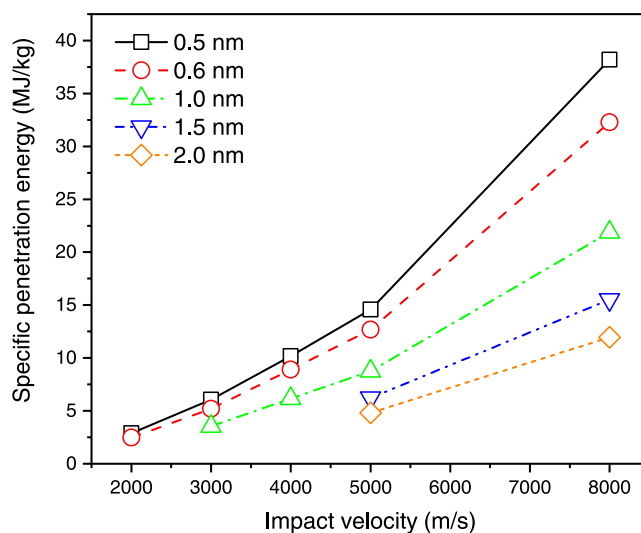


Figure 5. Specific penetration energy (E_p^*) of the Ni₂Ta MG nanofilms with different thicknesses and impact velocities from MD simulations. For 1.5-nm-thick and 2.0-nm-thick films, the films are not fully penetrated at impact velocities lower than 5 km s⁻¹.

film reaches an incredible 40 MJ kg⁻¹, which is about four times that of the 2-nm-thick film at the same impact velocity.

The ultrahigh impact resistance of the Ni₂Ta MG nanofilm should be contributed by the size-dependent mechanical behavior at small scales.^{15,16,26–29} The strength and ductility of the nanoscale film increase significantly compared to its bulk state due to the considerable reduction of inner defects and the larger proportion of surface energy. Once the particle impacts the target, the center of the film is under compressive stress, while the surrounding is under tensile stress. The propagation of the tensile wave leads to the continuous expansion of the conical deformation of the film (Figure 6), which provides the main impact energy dissipation channel. The typical perforation process for the Ni₂Ta metallic glass film is depicted in Figure 7. The film shows large plasticity as evidenced by the clear conic deformation during propagation of the stress waves followed by the occurrence of microvoids when the high-amplitude tensile stress exceeds the Hugoniot elastic limit (HEL), resulting in a circular crack due to the growth, gathering, and coalescence of the microvoids. The perforation hole of the Ni₂Ta MG film is larger than the strike-face area as observed in the experiments, indicating fast delocalized energy dissipation of the nanofilms. Both the ultrahigh strength and relatively large plasticity of the Ni₂Ta MG nanofilm lead to excellent impact resistance of the film. Due to the small size of the film and high impact velocity in the MD simulations, the Ni₂Ta MG nanofilms experience almost homogeneous plastic flow in the MD simulation rather than shear bands (Figure 8). During impact, a local region of the film stretches dramatically during impact leading to cavitation, which leads to the ultimate failure of the film. Although the MD simulation does not provide insights about the shear band deformation observed in experiments, the MD predicts the impact resistance and deformation mechanisms of the Ni₂Ta MG nanofilms at much smaller scales and higher impact velocities compared to experiments.

The local phase transformation of the Ni₂Ta MG nanofilm during impact also contributes to the impact resistance. Under impact-induced adiabatic heating, the temperature rise of the strike-face area of the film exceeds the melting temperature $T_m =$

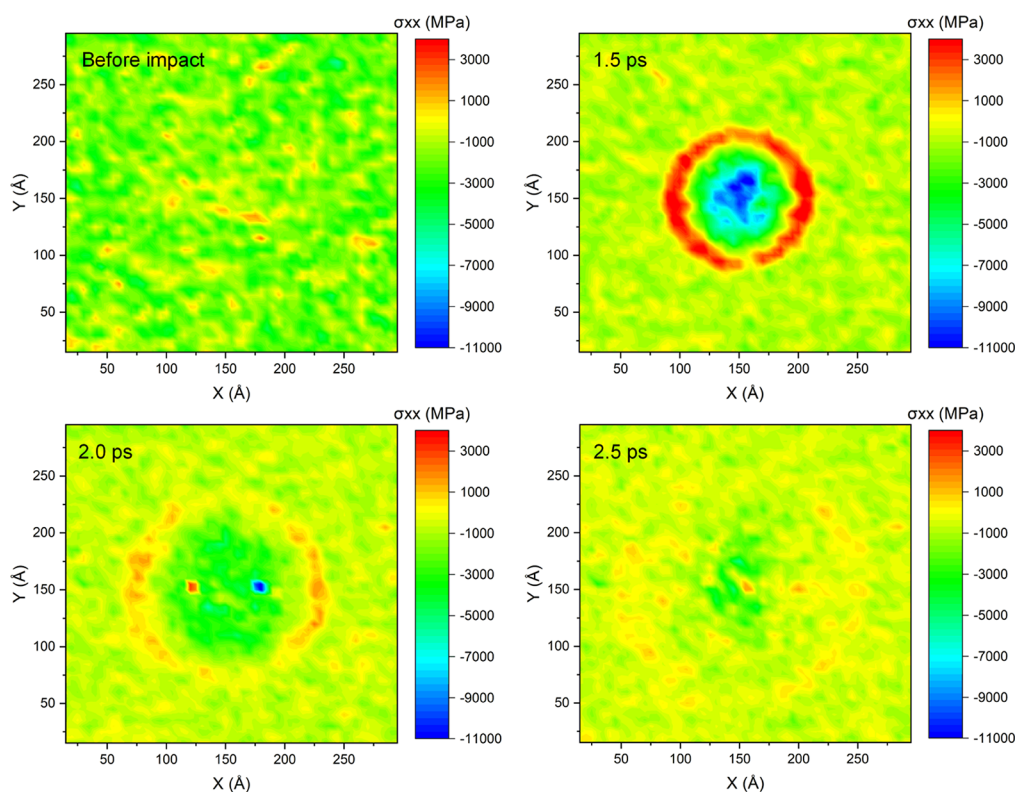


Figure 6. Stress wave propagation (σ_{xx}) from MD simulations of the MG nanofilm with a thickness of 3 nm at impact velocity $v_i = 4 \text{ km s}^{-1}$.

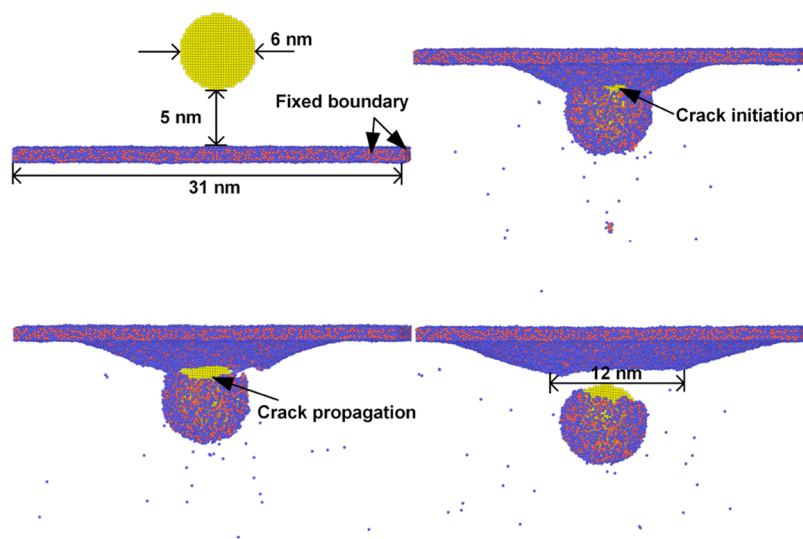


Figure 7. Deformation and failure mechanism from MD simulations of the Ni_2Ta MG nanofilm with a thickness of 1 nm at impact velocity $v_i = 3 \text{ km s}^{-1}$.

1800 K of the Ni_2Ta crystal structure (Figure S7), leading to melting of the film in the impact region, providing an additional dissipation channel for the impact energy. However, no crystallization is observed after impact as also observed in experiments.

To understand the thermal behavior of the nanofilm, we performed nonequilibrium molecular dynamics (NEMD) simulations to obtain the thermal conductivity of the Ni_2Ta MG nanofilm,

$$k = -dQ/(dT/dX) \quad (4)$$

The simulation results show that the Ni_2Ta MG nanofilm has a high thermal conductivity of $k = 9.7 \text{ w (m K)}^{-1}$, and it experiences an ultrafast cooling process with a rate over 10^{13} K s^{-1} as depicted in Figure 9, leading to the amorphous state as observed in experiments. The temperature at the center of the film has been corrected by subtracting the center of mass velocity. In this paper, our force field-based MD simulations consider only the lattice vibration contributions to the thermal conductivity of the Ni_2Ta MG nanofilms. Including the electronic contributions would lead to a larger thermal conductivity. The predicted thermal conductivity obtained by the present MD simulation can be regarded as a lower bound. As

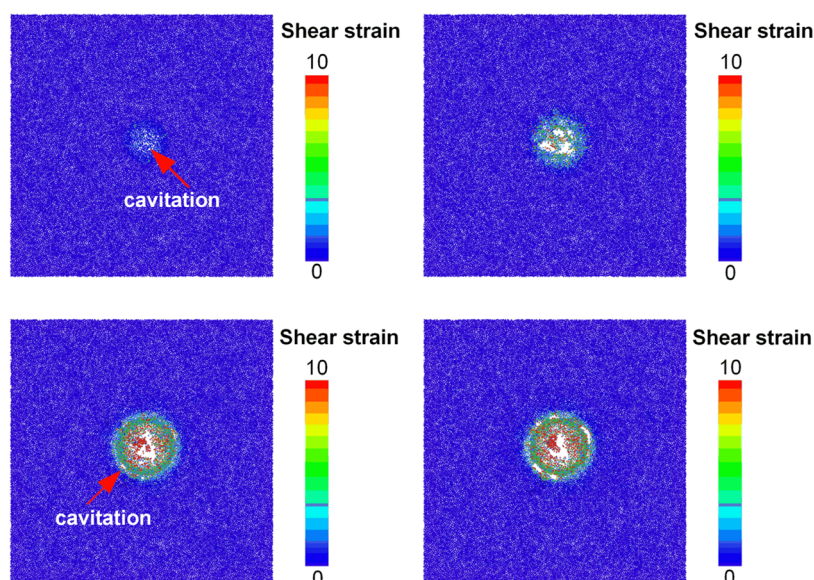


Figure 8. Deformation behavior and shear strain distribution of the Ni₂Ta MG nanofilm with a thickness of 1 nm at the impact velocity $v_i = 3 \text{ km s}^{-1}$.

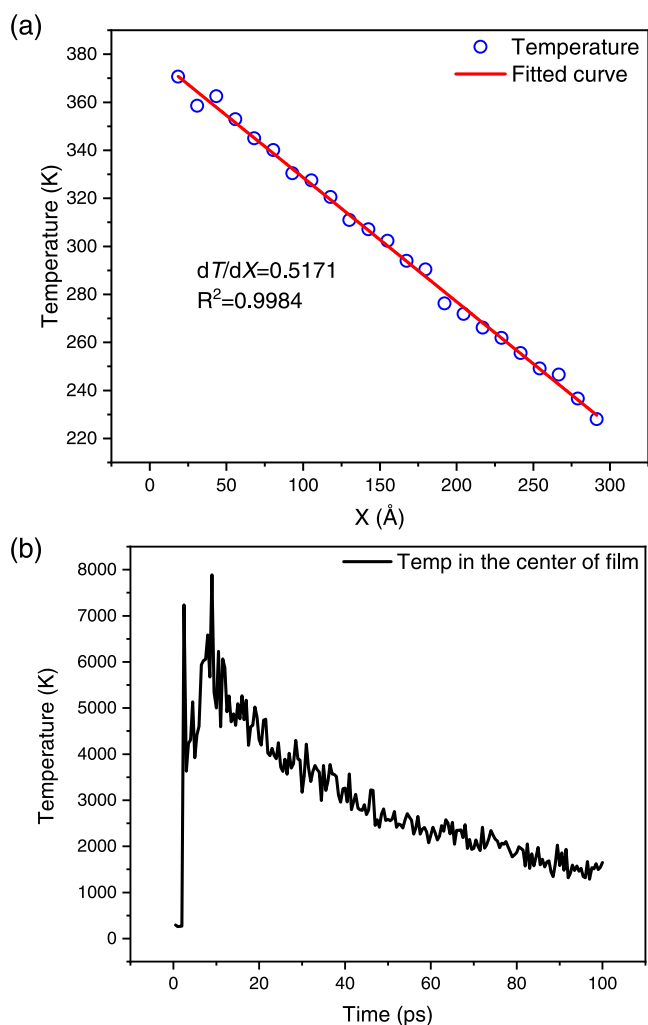


Figure 9. (a) Radial distribution of temperature of the Ni₂Ta MG nanofilm from MD simulations. This was used to estimate the thermal conductivity k of the Ni₂Ta MG nanofilm, leading to $k = 9.7 \text{ w (m k)}^{-1}$. (b) Temperature evolution at the center of the Ni₂Ta MG nanofilm during impact from MD simulations.

a result, we can conclude that the high thermal conductivity of the Ni₂Ta film limits the formation of the crystalline region.

Scaling Law for the Amorphous Alloy Film. There is a significant gap in the aspects of impact duration and thickness between experiments (0.2–2 ns, 60–600 nm) and MD simulations (0.1–10 ps, 0.5–3 nm). To bridge this gap to establish a means for predicting the impact resistance of amorphous films at various scales, we investigated the scaling law of the amorphous alloy film for impact resistance under high loading rates utilizing dimensional analysis, by which the dimensionless impact resistance $\frac{E_p^*}{v^2}$ of the film is determined by the dimensionless thickness d/h and dimensionless strength $\frac{\sigma_{b0}}{\rho v^2}$,

$$\frac{E_p^*}{v^2} = f\left(\frac{d}{h}, \frac{\sigma_{b0}}{\rho v^2}\right) \quad (5)$$

where ρ , d , and v are the density, diameter, and initial impact velocity of the micro-bullet; h is the thickness of the film; and σ_{b0} is the macroscopic tensile strength of the film under quasi-static loading rate.

From eq 5, the dimensionless specific energy absorption is determined by the dimensionless thickness and dimensionless strength of the film. Assuming the influence of the dimensionless thickness d/h and the dimensionless strength $\sigma_{b0}/\rho v^2$ are independent, their effect has a product form,

$$\frac{E_p^*}{v^2} = \zeta\left(\frac{d}{h}\right)\xi\left(\frac{\sigma_{b0}}{\rho v^2}\right) \quad (6)$$

Clearly, there is a geometrical scaling law for the impact resistance of the amorphous alloy film. If we keep $\sigma_{b0}/\rho v^2$ constant, but change the diameter d of the micro-bullet and the thickness h of the film with the same proportion, the dimensionless impact resistance E_p^*/v^2 will remain the same, which is validated by MD simulations (see Table S4 in the Supporting Information).

Based on a large number of MD simulations, the specific expressions of the functions $\zeta(d/h)$ and $\xi\left(\frac{\sigma_{b0}}{\rho v^2}\right)$ are obtained as

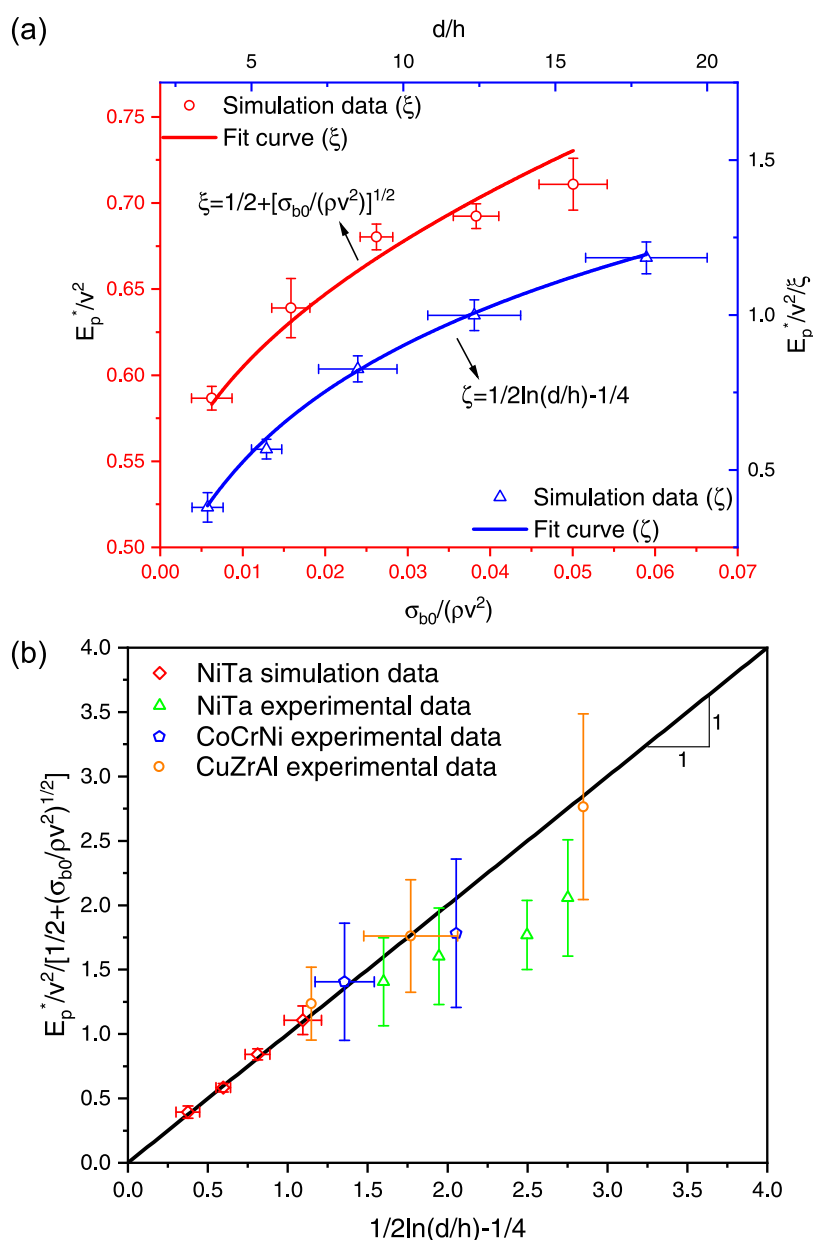


Figure 10. (a) Influence of $\sigma_{b0}/\rho v^2$ and d/h on E_p^*/v^2 at MD simulation scale. By fixing $d/h = 12$ ($d = 6$ nm, $h = 0.5$ nm), the relationship between E_p^*/v^2 and $\sigma_{b0}/\rho v^2$ is obtained. Then, fixing the impact velocity to 5 km s^{-1} , the relationship between $E_p^*/v^2 \xi$ and d/h is obtained. (b) Comparison of the micro-ballistic impact experimental and MD simulation results with the dimensionless equation [eq 9], which is represented by the straight line.

follows. First, we keep $d/h = 12$ ($d = 6$ nm, $h = 0.5$ nm) and change $\sigma_{b0}/\rho v^2$, the relationship between E_p^*/v^2 and $\sigma_{b0}/\rho v^2$ are shown in Figure 10a, which can be fitted with a power function,

$$\xi \left(\frac{\sigma_{b0}}{\rho v^2} \right) = \alpha + \left(\frac{\sigma_{b0}}{\rho v^2} \right)^\beta \quad (7)$$

where $\alpha = 1/2$ and $\beta = 1/2$. In this paper, the characteristic tensile strength σ_{b0} is defined as the tensile strength of the material at macroscopic scale under quasi-static loading rates. Therefore, it is independent of the strain rate. The macroscopic strength of bulk Ni_2Ta MG rods with a diameter of 2 mm is about 3 GPa using a quasi-static compression test.¹⁷ Thus, we take the characteristic tensile strength σ_{b0} as 3 GPa. Then, we keep $\sigma_{b0}/\rho v^2 = 0.0088$ (the impact velocity $v = 5 \text{ km s}^{-1}$) and change d/h , leading to the relationship between $\frac{E_p^*}{v^2} / \xi \left(\frac{\sigma_{b0}}{\rho v^2} \right)$ and

d/h (Figure 10a), which can be fitted with a logarithmic function,

$$\xi \left(\frac{d}{h} \right) = \gamma \ln \frac{d}{h} - \delta \quad (8)$$

where $\gamma = 1/2$ and $\delta = 1/4$. Equation 8 applies to the condition $d/h \geq e^{1/2}$. Otherwise, it would not be a thin-film impact problem that is considered in the present study.

From eqs 7 and 8, we derive the following empirical formula

$$\frac{E_p^*}{v^2} = \left[\frac{1}{2} + \left(\frac{\sigma_{b0}}{\rho v^2} \right)^{1/2} \right] \left[\frac{1}{2} \ln \frac{d}{h} - \frac{1}{4} \right] \quad (9)$$

Figure 10b shows all simulation and experimental results for the Ni_2Ta MG film. The straight line represents eq 9. Despite a significant gap in the impact duration and film thickness between

experiments (0.2–2 ns, 60–600 nm) and MD simulations (0.1–10 ps, 0.5–3 nm), we see that the simulation results and the experimental results both follow the same rule described by eq 9 when the value of d/h is smaller than 2.0. For d/h values larger than 2.0, the experimental results begin to deviate from the predicted results for Ni₂Ta MG nanofilms. This may indicate some other mechanisms at larger d/h or it could indicate that the relationship is not linear. In addition, we performed micro-ballistic impact experiments on two other amorphous alloys (Cu_{47.5}Zr_{47.5}Al₅ and CoCrNi) films as shown in Figure 10b. It is interesting to note that the results on these two films also obey the same rule found for the Ni₂Ta MG film, indicating that eq 9 may be universal for describing the size-dependent multiscale impact resistance of amorphous alloy films. These results also validate that the scaling law remains applicable at the atomistic scale, bridging the gap between MD simulations and micro-ballistic impact experiments. In the regime of ballistic impact, the strength and ductility of material play significant roles.^{32,33} Although the mechanical behavior of a film at a level of atomistic simulations varies markedly due to the size effects,^{15,16,26–29} the impact resistance of the nanofilm should still be determined by the strength and ductility. Therefore, we can scale successfully the impact resistance of amorphous alloy films between MD simulations and micro-ballistic impact experiments. The present study provides guidance for fabricating amorphous alloy films with extraordinary impact resistance and a method for predicting its impact resistance at various scales in the protective structure design.

CONCLUSIONS

In this work, we provide the first examples of the dynamic size effects of amorphous films based on micro-ballistic impact experiments and MD simulations. The impact resistance increases rapidly with increasing impact velocity and decreasing thickness of the amorphous nanofilm. This dynamic size effect of the amorphous films is related to the surface energy and the inner defects, rendering a higher strength, and larger ductility at a small scale. On the basis of dimensional analysis, we obtained a scaling law for impact resistance of amorphous alloy films, which describes successfully the size-dependent multiscale impact resistance of the amorphous alloys. Our work establishes a universal method for predicting the impact resistance of amorphous alloy films and provides a guideline for fabricating high-performance amorphous alloy films with extraordinary impact resistance.

MATERIALS AND METHODS

Materials. The Ni₂Ta MG was fabricated by ion-beam-assisted deposition (IBAD). First, an 80-nm-thick aluminum (Al) layer was deposited on a flat polycarbonate (PC) plate with a diameter of 10 cm and a thickness of 0.3 mm. Then, a series Ni₂Ta MG films with a thickness varying from 100 to 600 nm (Figure S8) were deposited on the top surface of the Al layer by controlling ion beam deposition time from 1000 to 6000 s. The ion beam energy is 750 mV, and the ion beam current is 50 mA. The base pressure of the chamber is 2×10^{-4} Pa, and the depositing argon pressure is 2.4×10^{-2} Pa. The Ni₂Ta MG nanofilm was detached from the PC substrate by dissolving the in-between Al layer with 1 mol L⁻¹ NaOH solution, and then the impurities on the nanofilm were removed using deionized water. After that, the Ni₂Ta MG nanofilm was transferred to and attached with 100 mesh transmission electron microscopy (TEM) copper grids as the impact targets. The Ni₂Ta MG nanofilm within a $280 \times 280 \mu\text{m}^2$ grid is free-standing and unsupported. Figure S9 shows the high-resolution TEM image of the Ni₂Ta MG nanofilm with different thicknesses. The typical

speckle pattern stemming from scattering at an amorphous structure of films with different thicknesses is clearly observed, which is consistent with the featureless halo observed by selected-area electron diffraction (SEAD) as shown in the inset.

Micro-Ballistic Impact Experiments. The launchpad of the LIPIT consists of a 4-mm-thick K9 glass substrate, a 40- μm -thick Al film, and a 70- μm -thick poly(dimethylsiloxane) (PDMS) elastomer film. A single Al micro-bullet with a diameter of $25 \pm 2 \mu\text{m}$ is attached to the free surface of the launchpad. A single laser pulse excited by a Q-switched Nd:YAG laser with a wavelength of 1064 nm and a full width at half-maximum (FWHM) of 10 ns is focused into a 1-mm-diameter spot size to irradiate the Al film, leading to the generation and rapid expansion of the plasma that finally accelerates a single micro-bullet to a supersonic speed due to the fast swelling of the PDMS film. The launch speed of the micro-particle is adjusted to vary from 300 to 500 m s⁻¹ by changing the laser pulse energy. The PDMS layer also serves as an effective thermal barrier between the high-temperature ablation-generated plasma and the micro-bullet so that it is maintained at the pre-launch temperature.

The supersonic micro-ballistic impact results in high-strain-rate (10^8 s⁻¹) deformation of the nanofilms. Due to the short penetration duration and large ratio of TEM grid length to the diameter of micro-bullets, the influence of the boundary conditions of the film is negligible. The impact process is in situ, real-time captured using a high-speed SI Kirana camera (Specialised Imaging, U.K.) with a NAVITAR microscope objective lens (12 \times magnification, 34 cm focal length). An SI-LUX laser unit (640 nm wavelength, 10 μs duration) is used for illumination. The inter-frame time is 200 ns, and the exposure time is 100 ns.

MD Simulations. The MD simulations were performed using the large-scale atomistic/molecular massively parallel simulator (LAMMPS) code.³⁴ The Open Visualization Tool (OVITO) software is used to visualize the atomistic configurations.³⁵ Validated interatomic potentials or force fields are essential to accurate atomistic simulations. Therefore, we adopt the embedded atom method (EAM) potential, which has adequate accuracy for predicting the properties of metallic systems. The EAM interaction potential between Ni and Ta was derived from a recently developed alloy EAM potential database, for which the alloy potentials can be determined by the normalized elemental potentials.³⁶ Before the simulation, we verified the EAM potentials³⁶ of the Ni₂Ta system. The results show that the EAM potential is appropriate for the present study^{37–39} (see the Supporting Information). We first melted the system completely by heating to 2500 K for 0.3 ns, followed by a rapid cooling procedure at a rate of about 7×10^{11} K s⁻¹⁴⁰ (see preparation process in the Supporting Information), to obtain Ni₂Ta MG films with in-plane dimensions of $31 \times 31 \text{ nm}^2$ and a thickness ranging from 0.5 to 3 nm.

Based on numerical simulations (Figure S3 in the Supporting Information) and experimental observations, there should be no obvious plastic deformation and fracture of the micro-bullet before and after penetration in experiments. As a result, we regard the Al micro-bullet as rigid in MD simulations to improve the computational efficiency. We adopted a Lennard-Jones (LJ) potential (6–12) to describe the interaction between the bullet and the target. The potential parameters are fitted according to the equilibrium distance and cohesive energy curves^{41,42} (see Table S5 in the Supporting Information). Fixed boundary conditions were applied on the peripheries of the film during impact. The lengths of the nanofilms are more than 5 times the diameter of the bullet to diminish boundary effects. The initial distance between the bullet and the film is 50 Å to avoid initial interactions. We employed the velocity-Verlet time-step method with a 1 fs timestep in all simulations. Initially, the bullet was fixed and the system was fully relaxed using conjugate gradient energy minimization. To obtain the thermal equilibrium state under the NVT ensemble, the models were equilibrated for 3 ns. After that, we used the microcanonical ensemble (i.e., NVE) to describe the normal penetration behavior of the Ni₂Ta films under the impact of the rigid bullet. Due to the limitations on the number of atoms in the MD simulations, the diameter of the rigid ball and the size of the film in the simulation are much smaller than those in the experiment. Since thinner films exhibit better impact resistance,

higher impact velocities ranging from 2 to 8 km s⁻¹ are used to ensure full perforation of the film, allowing the specific energy absorption of the film to be determined at the nanoscale.

Dimensional Analysis. According to the Buckingham Π theorem,⁴³ a physical process can be described by a dependent variable, a_0 , and n independent variables, $a_1, a_2, a_3, \dots, a_n$, as follows

$$a_0 = f(a_1, a_2, a_3, \dots, a_n) \quad (10)$$

where f is the function of the physical process. If the number of fundamental quantities is m (e.g., fundamental quantities: $a_1, a_2, a_3, \dots, a_m$), then eq 10 can be rewritten as

$$\frac{a_0}{a_1^{b_1} a_2^{b_2} \dots a_m^{b_m}} = f \left(\underbrace{1, 1, \dots, 1}_m; \frac{a_{m+1}}{a_1^{p_1} a_2^{p_2} \dots a_m^{p_m}}, \frac{a_{m+2}}{a_1^{q_1} a_2^{q_2} \dots a_m^{q_m}}, \dots, \frac{a_n}{a_1^{r_1} a_2^{r_2} \dots a_m^{r_m}} \right) \quad (11)$$

The parameters that affect the impact resistance E_p^* include:

- the density ρ , the diameter d , and the initial impact velocity v of the micro-bullet, and
- the density ρ_0 , the thickness h , the Poisson ratio ν , the elastic modulus E_0 , the tensile strength σ_b , and the failure strain ε_f of the film.

The deformation mechanism of MG films changes depending on the impact velocities. At low impact velocities, the film exhibits plastic deformation carried by shear bands, while at high velocities the film exhibits higher levels of adiabatic heating and eventually uniform plastic flow. Therefore, we include the effects of strain rate in the dimensional analysis. For the impact problem, we find that the tensile strength and the failure strain, which determine the maximum strain energy of a material, dominate the impact resistance of a film. In dimensional analysis, the tensile strength, σ_b , of the film depends on its thickness (h) and strain rate (v/h) as $\sigma_b = \sigma_{b0} g(h, v/h)$, where the constant, σ_{b0} , is the characteristic tensile strength of the film, which can be regarded as the macroscale tensile strength under quasi-static loading rate (about 3 GPa) without loss of generality. Similarly, the failure strain, ε_f , of the thin film can be written as $\varepsilon_f = \varepsilon_{f0} g'(h, v/h)$, where, ε_{f0} , is the characteristic failure strain of the film, which can also be regarded as the macroscale failure strain under quasi-static loading rates. Therefore, we include the strain-rate-dependent penetration behavior and size effects of the film.

Therefore, the impact resistance of the film is a function of these parameters,

$$E_p^* = f(\rho, \rho_0, d, h, v, E_0, \sigma_{b0}, \varepsilon_{f0}, \nu) \quad (12)$$

Taking density ρ , thickness h , and initial impact velocity v as independent variables, we obtain the following equation

$$\frac{E_p^*}{v^2} = f \left(\frac{\rho_0}{\rho}, \frac{d}{h}, \frac{\sigma_{b0}}{E_0}, \frac{\sigma_{b0}}{\rho v^2}, \varepsilon_{f0}, \nu \right) \quad (13)$$

In this study, the dimensionless parameter $\frac{E_p^*}{v^2}$ represents the ratio between the absorbed energy per unit mass of the film and the initial energy per unit mass of the micro-bullet, indicating the energy transmission efficiency of the film. If the materials of the micro-bullet and the thin film are not changed, the dimensionless parameters ρ_0/ρ , σ_{b0}/E_0 , ε_{f0} , and ν are constants. As a result, eq 13 can be rewritten as

$$\frac{E_p^*}{v^2} = f \left(\frac{d}{h}, \frac{\sigma_{b0}}{\rho v^2} \right) \quad (14)$$

MG amorphous alloys have disordered structures. For MG films with thicknesses smaller than 600 nm as employed in LPIT experiments and MD simulations, it is hard to form macroscopic defects so that the films can be regarded as defect-free materials. Therefore, we do not consider the influence of defects in simulations and dimensional analysis.

However, with increasing the thickness of the MG films, some macroscopic defects may appear, which will be investigated in the future.

■ ASSOCIATED CONTENT

SI Supporting Information

The Supporting Information is available free of charge at <https://pubs.acs.org/doi/10.1021/acsami.2c19719>.

Additional details of experiments, materials, and numerical simulation methods (PDF)

■ AUTHOR INFORMATION

Corresponding Authors

Xianqian Wu – Key Laboratory of Mechanics in Fluid Solid Coupling Systems, Institute of Mechanics, Chinese Academy of Sciences, Beijing 100190, China; School of Engineering Science, University of Chinese Academy of Sciences, Beijing 100049, China; orcid.org/0000-0001-5824-2203; Email: wuxianqian@imech.ac.cn

William A. Goddard, III – Materials and Process Simulation Center, California Institute of Technology, Pasadena, California 91125, United States; orcid.org/0000-0003-0097-5716; Email: wag@caltech.edu

Authors

Yujie Cheng – Key Laboratory of Mechanics in Fluid Solid Coupling Systems, Institute of Mechanics, Chinese Academy of Sciences, Beijing 100190, China; School of Engineering Science, University of Chinese Academy of Sciences, Beijing 100049, China

Jinlei Dong – Key Laboratory of Mechanics in Fluid Solid Coupling Systems, Institute of Mechanics, Chinese Academy of Sciences, Beijing 100190, China; Institute of Fluid Physics, CAEP, Mianyang 621999, China

Fucheng Li – Institute of Physics, Chinese Academy of Sciences, Beijing 100190, China

Yidi Shen – Department of Materials Science and Engineering, Iowa State University, Ames, Iowa 50011, United States

Qi An – Department of Materials Science and Engineering, Iowa State University, Ames, Iowa 50011, United States; orcid.org/0000-0003-4838-6232

Kailu Xiao – Key Laboratory of Mechanics in Fluid Solid Coupling Systems, Institute of Mechanics, Chinese Academy of Sciences, Beijing 100190, China; School of Engineering Science, University of Chinese Academy of Sciences, Beijing 100049, China; orcid.org/0000-0001-5013-7951

Minqiang Jiang – School of Engineering Science, University of Chinese Academy of Sciences, Beijing 100049, China; State Key Laboratory of Nonlinear Mechanics, Institute of Mechanics, Chinese Academy of Sciences, Beijing 100190, China

Yanhui Liu – Institute of Physics, Chinese Academy of Sciences, Beijing 100190, China

Chenguang Huang – School of Engineering Science, University of Chinese Academy of Sciences, Beijing 100049, China

Complete contact information is available at:

<https://pubs.acs.org/doi/10.1021/acsami.2c19719>

Author Contributions

Y.C., J.D., and F.L. contributed equally to this work. X.W. and W.A.G. designed research. Y.C. performed MD simulation. Q.A., Y.S., and W.A.G. obtained force field. J.D. performed

impact experiments. F.L. prepared materials. K.X., X.W., M.J., Y.L., and C.H. analyzed data. Y.C., X.W., Q.A., and W.A.G. wrote the paper. All authors reviewed the manuscript.

Notes

The authors declare no competing financial interest.

ACKNOWLEDGMENTS

X.W. acknowledges support from National Natural Science Foundation of China (12272391, 12232020). W.A.G. acknowledges support from ONR (N00014-19-1-2081).

REFERENCES

- (1) Lee, J. H.; Loya, P. E.; Lou, J.; Thomas, E. L. Dynamic Mechanical Behavior of Multilayer Graphene Via Supersonic Projectile Penetration. *Science* **2014**, *346*, 1092–1096.
- (2) Hassani-Gangaraj, M.; Veysset, D.; Nelson, K. A.; Schuh, C. A. Melt-Driven Erosion in Microparticle Impact. *Nat. Commun.* **2018**, *9*, No. 5077.
- (3) Chan, E. P.; Xie, W.; Orski, S. V.; Lee, J. H.; Soles, C. L. Entanglement Density-Dependent Energy Absorption of Polycarbonate Films Via Supersonic Fracture. *ACS Macro Lett.* **2019**, *8*, 806–811.
- (4) Greer, J. R.; De Hosson, J. T. M. Plasticity in Small-Sized Metallic Systems: Intrinsic Versus Extrinsic Size Effect. *Prog. Mater. Sci.* **2011**, *56*, 654–724.
- (5) Bauer, J.; Meza, L. R.; Schaedler, T. A.; Schwaiger, R.; Zheng, X.; Valdevit, L. Nanolattices: An Emerging Class of Mechanical Metamaterials. *Adv. Mater.* **2017**, *29*, No. 1701850.
- (6) Qiao, J.; Jia, H.; Liaw, P. K. Metallic Glass Matrix Composites. *Mater. Sci. Eng., R* **2016**, *100*, 1–69.
- (7) Reddy, K. V.; Deng, C.; Pal, S. Dynamic Characterization of Shock Response in Crystalline-Metallic Glass Nanolaminates. *Acta Mater.* **2019**, *164*, 347–361.
- (8) Wang, W. H. Dynamic Relaxations and Relaxation-Property Relationships in Metallic Glasses. *Prog. Mater. Sci.* **2019**, *106*, No. 100561.
- (9) Hufnagel, T. C.; Schuh, C. A.; Falk, M. L. Deformation of Metallic Glasses: Recent Developments in Theory, Simulations, and Experiments. *Acta Mater.* **2016**, *109*, 375–393.
- (10) Di, S.; Wang, Q.; Zhou, J.; Shen, Y.; Li, J.; Zhu, M.; Yin, K.; Zeng, Q.; Sun, L.; Shen, B. Enhancement of Plasticity for Fecobsinb Bulk Metallic Glass with Superhigh Strength through Cryogenic Thermal Cycling. *Scr. Mater.* **2020**, *187*, 13–18.
- (11) Huang, X.; Ling, Z.; Liu, Z. D.; Zhang, H. S.; Dai, L. H. Amorphous Alloy Reinforced Whipple Shield Structure. *Int. J. Impact Eng.* **2012**, *42*, 1–10.
- (12) Hofmann, D. C.; Hamill, L.; Christiansen, E.; Nutt, S. Hypervelocity Impact Testing of a Metallic Glass-Stuffed Whipple Shield. *Adv. Eng. Mater.* **2015**, *17*, 1313–1322.
- (13) Dong, J. L.; Song, X.; Wang, Z. J.; Xiao, K. L.; Liu, Y. H.; Wilde, G.; Wu, X. Q.; Jiang, M. Q. Impact Resistance of Single-Layer Metallic Glass Nanofilms to High-Velocity Micro-Particle Penetration. *Extreme Mech. Lett.* **2021**, *44*, No. 101258.
- (14) Guo, H.; Yan, P. F.; Wang, Y. B.; Tan, J.; Zhang, Z. F.; Sui, M. L.; Ma, E. Tensile Ductility and Necking of Metallic Glass. *Nat. Mater.* **2007**, *6*, 735–739.
- (15) Kumar, G.; Desai, A.; Schroers, J. Bulk Metallic Glass: The Smaller the Better. *Adv. Mater.* **2011**, *23*, 461–476.
- (16) Jang, D.; Greer, J. R. Transition from a Strong-yet-Brittle to a Stronger-and-Ductile State by Size Reduction of Metallic Glasses. *Nat. Mater.* **2010**, *9*, 215–219.
- (17) Wang, Y.; Wang, Q.; Zhao, J.; Dong, C. Ni–Ta Binary Bulk Metallic Glasses. *Scr. Mater.* **2010**, *63*, 178–180.
- (18) Veysset, D.; Hsieh, A. J.; Kooi, S.; Maznev, A. A.; Masser, K. A.; Nelson, K. A. Dynamics of Supersonic Microparticle Impact on Elastomers Revealed by Real-Time Multi-Frame Imaging. *Sci. Rep.* **2016**, *6*, No. 25577.
- (19) Hassani-Gangaraj, M.; Veysset, D.; Nelson, K. A.; Schuh, C. A. Melting Can Hinder Impact-Induced Adhesion. *Phys. Rev. Lett.* **2017**, *119*, No. 175701.
- (20) Cai, J.; Thevamaran, R. Superior Energy Dissipation by Ultrathin Semicrystalline Polymer Films under Supersonic Microprojectile Impacts. *Nano Lett.* **2020**, *20*, 5632–5638.
- (21) Dewapriya, M. A. N.; Miller, R. E. Superior Dynamic Penetration Resistance of Nanoscale Multilayer Polymer/Metal Films. *J. Appl. Mech.* **2020**, *87*, No. 121009.
- (22) Hyon, J.; Lawal, O.; Fried, O.; Thevamaran, R.; Yazdi, S.; Zhou, M.; Veysset, D.; Kooi, S. E.; Jiao, Y.; Hsiao, M.-S.; Streit, J.; Vaia, R. A.; Thomas, E. L. Extreme Energy Absorption in Glassy Polymer Thin Films by Supersonic Micro-Projectile Impact. *Mater. Today* **2018**, *21*, 817–824.
- (23) Zeng, F.; Jiang, M. Q.; Dai, L. H. Dilatancy Induced Ductile-Brittle Transition of Shear Band in Metallic Glasses. *Proc. R. Soc. London, Ser. A* **2018**, *474*, No. 20170836.
- (24) Schuh, C.; Hufnagel, T.; Ramamurty, U. Mechanical Behavior of Amorphous Alloys. *Acta Mater.* **2007**, *55*, 4067–4109.
- (25) Pan, D.; Inoue, A.; Sakurai, T.; Chen, M. W. Experimental Characterization of Shear Transformation Zones for Plastic Flow of Bulk Metallic Glasses. *Proc. Natl. Acad. Sci. U.S.A.* **2008**, *105*, 14769–14772.
- (26) Adibi, S.; Branicio, P. S.; Lontas, R.; Chen, D. Z.; Greer, J. R.; Srolovitz, D. J.; Joshi, S. P. Surface Roughness Imparts Tensile Ductility to Nanoscale Metallic Glasses. *Extreme Mech. Lett.* **2015**, *5*, 88–95.
- (27) Zhou, X.; Zhou, H.; Li, X.; Chen, C. Size Effects on Tensile and Compressive Strengths in Metallic Glass Nanowires. *J. Mech. Phys. Solids* **2015**, *84*, 130–144.
- (28) Kuroyanagi, S.; Shinoda, K.; Yumoto, A.; Akedo, J. Size-Dependent Quasi Brittle–Ductile Transition of Single Crystalline Alpha-Alumina Particles During Microcompression Tests. *Acta Mater.* **2020**, *195*, 588–596.
- (29) Wang, N.; Cao, Q. P.; Yao, W.; Wang, X. D.; Zhang, D. X.; Fecht, H. J.; Jiang, J. Z. Anisotropic and Size-Dependent Mechanical Responses of Free-Standing Ni–Nb Metallic Glass Thin Film. *Scr. Mater.* **2021**, *198*, No. 113832.
- (30) Greer, A. L.; Cheng, Y. Q.; Ma, E. Shear Bands in Metallic Glasses. *Mater. Sci. Eng., R* **2013**, *74*, 71–132.
- (31) Chen, Y.; Jiang, M. Q.; Dai, L. H. Collective Evolution Dynamics of Multiple Shear Bands in Bulk Metallic Glasses. *Int. J. Plast.* **2013**, *50*, 18–36.
- (32) Duffey, T.; Cheresh, M.; Sutherland, S. Experimental Verification of Scaling Laws for Punch-Impact-Loaded Structures. *Int. J. Impact Eng.* **1984**, *2*, 103–117.
- (33) Ryan, S.; Nguyen, L. H.; Gallardy, D.; Cimpoeu, S. J. A Scaling Law for Predicting the Ballistic Limit of Aluminium Alloy Targets Perforated in Ductile Hole Formation. *Int. J. Impact Eng.* **2018**, *116*, 34–50.
- (34) Plimpton, S. Fast Parallel Algorithms for Short-Range Molecular Dynamics. *J. Comput. Phys.* **1995**, *117*, 1–19.
- (35) Zepeda-Ruiz, L. A.; Stukowski, A.; Opperstrup, T.; Bulatov, V. V. Probing the Limits of Metal Plasticity with Molecular Dynamics Simulations. *Nature* **2017**, *550*, 492–495.
- (36) Zhou, X. W.; Johnson, R. A.; Wadley, H. N. G. Misfit-Energy-Increasing Dislocations in Vapor-Deposited CoFe/NiFe Multilayers. *Phys. Rev. B* **2004**, *69*, No. 144113.
- (37) Zhou, Y.; Wen, B.; Ma, Y.; Melnik, R.; Liu, X. First-Principles Studies of Ni–Ta Intermetallic Compounds. *J. Solid State Chem.* **2012**, *187*, 211–218.
- (38) Zhang, C.; Yuan, J.; Ye, C.; Liao, B.; Zhang, Z.; Xiang, H.; Chen, L. First-Principles Study on the Mechanical, Vibrational and Thermodynamic Characteristics of Intermetallic Compound Ni₂Ta. *Phys. B* **2020**, *578*, No. 411888.
- (39) Nash, A.; Nash, P. The Ni–Ta (Nickel–Tantalum) System. *Bull. Alloy Phase Diagrams* **1984**, *5*, 259–265.
- (40) Zhang, F.; Mendelev, M. I.; Zhang, Y.; Wang, C. Z.; Kramer, M. J.; Ho, K. M. Effects of Sub-Tg Annealing on Cu_{64.5}Zr_{35.5} Glasses: A Molecular Dynamics Study. *Appl. Phys. Lett.* **2014**, *104*, No. 061905.

(41) Kang, Y. M.; Chen, N. X.; Shen, J. Atomistic Simulation of the Lattice Constants and Lattice Vibrations in Rt_4Al_8 (R=Nd, Sm; T=Cr, Mn, Cu, Fe). *J. Alloys Compd.* **2003**, *352*, 26–33.

(42) Kang, Y. M.; Chen, N. X.; Shen, J. Site Preference and Vibrational Properties of Ni_3Al with Ternary Additions Pd and Ag. *Mod. Phys. Lett. B* **2002**, *16*, 727–737.

(43) Buckingham, E. On Physically Similar Systems, Illustrations of the Use of Dimensional Equations. *Phys. Rev.* **1914**, *4*, 345–376.

Recommended by ACS

Predicted Three-Dimensional Structure of the GCR1 Putative GPCR in *Arabidopsis thaliana* and Its Binding to Abscisic Acid and Gibberellin A1

Pedro M. Hernández, William A. Goddard III, *et al.*

MARCH 28, 2023
JOURNAL OF AGRICULTURAL AND FOOD CHEMISTRY

READ 

In Silico High-Throughput Design and Prediction of Structural and Electronic Properties of Low-Dimensional Metal–Organic Frameworks

Zeyu Zhang, Farnaz A. Shakib, *et al.*

FEBRUARY 07, 2023
ACS APPLIED MATERIALS & INTERFACES

READ 

Graphene-Supported Tin Single-Atom Catalysts for CO_2 Hydrogenation to HCOOH: A Theoretical Investigation of Performance under Different N Coordination Numbers

Xiaotao Liang, Xin Chen, *et al.*

MARCH 10, 2023
ACS APPLIED NANO MATERIALS

READ 

Ion Kinetics and Capacity Tailoring in Stacked Graphdiyne by Functionalization

Zixuan Zhu and Dongxing Song

FEBRUARY 20, 2023
ACS OMEGA

READ 

Get More Suggestions >